Modeling of stratospheric balloons and robust line-of-sight pointing control

Ervan Kassarian, Francesco Sanfedino, Daniel Alazard, Johan Montel, Charles-Antoine Chevrier

To cite this version:

Ervan Kassarian, Francesco Sanfedino, Daniel Alazard, Johan Montel, Charles-Antoine Chevrier. Modeling of stratospheric balloons and robust line-of-sight pointing control. CEAS Space Journal, 2024, 16, pp.457-474. ⟨10.1007/s12567-023-00515-x⟩. ⟨hal-04450280⟩

Modeling of stratospheric balloons and robust line-of-sight pointing control

Ervan Kassarian[1] · **Francesco Sanfedino**[2] · **Daniel Alazard**[2] · **Johan Montel**[3] · **Charles-Antoine Chevrier**[3]

Abstract

This paper investigates state-of-the-art modeling and control techniques for the robust line-of-sight pointing control of an optical payload on-board a stratospheric balloon, to meet stringent pointing requirements in the context of astronomy missions. Previous experience shows that the pointing performance of such systems is essentially limited by the rejection of the natural pendulum-like oscillations of the flight chain. This observation justifies the need for a model that accurately predicts such flight conditions that cannot be replicated in laboratory, and for a systematic methodology addressing the line-of-sight controller design to reject these flexible dynamics excited by wind disturbances. Moreover, it is sought to ensure robust stability and performance to the parametric uncertainties inherent to balloon-borne systems, such as complex balloon's properties or release of ballast throughout the flight, especially since experimental validation is limited. In this paper, a first dynamical model of the complete system is proposed, based on Lagrangian mechanics; the comparison with flight data show that the frequency content of the platform's motion is accurately predicted. Then, a multibody approach is applied to derive a second model taking into account the parametric uncertainties with the Linear Fractional Transformation representation. Finally, the control of the line-of-sight is tackled as a robust, structured $\mathcal{H}_2/\mathcal{H}_\infty$ problem that improves the performance with regard to traditional PID controller. A μ-sensitivity analysis is also proposed to identify the most sensitive parameters and verify the performance.

Keywords Stratospheric balloon · Line-of-sight pointing control · Robust control

1 Introduction

Reusable and flexible in their deployment and operability, while also cheaper, more ecological and with faster development times than satellites [1, chap.1.3], stratospheric balloons can carry heavy scientific payloads into the near-space environment for short duration missions. In particular, optical instruments benefit from the low atmospheric absorption at such altitudes, making stratospheric balloons suited for astronomy missions. Such missions typically have sub-arcsecond pointing precision requirements [2–7], and current developments aim at further improving the precision with fast-steering mirrors [8, 9]. To address more and more stringent precision objectives, it is necessary to develop accurate dynamical models and specific control strategies.

The earliest dynamical models of stratospheric balloon-borne systems are found in 1975 in a technical report from NASA [10] motivated by the attitude determination for the LACATE experiment, and developed further by the same authors [11–13]. About the vertical axis, the torsion of the

✉ Ervan Kassarian
ervan.kassarian@dycsyt.com

Francesco Sanfedino
francesco.sanfedino@isae.fr

Daniel Alazard
daniel.alazard@isae.fr

Johan Montel
johan.montel@cnes.fr

Charles-Antoine Chevrier
charlesantoine.chevrier@cnes.fr

[1] DYCSYT, 10 Avenue Edouard Belin, 31055 Toulouse, France

[2] ISAE-Supaero, 10 Avenue Edouard Belin, 31055 Toulouse, France

[3] CNES, 18 Avenue Edouard Belin, 31055 Toulouse, France

flight chain is traditionally modeled as a mass-spring system [14–22]. Although the stiffness is generally experimentally determined by system identification, which requires to deploy the whole system and process in-flight data, the bi-filar pendulum model allows predicting analytically the stiffness of balloon flight chains [23, 24]. About the two other axes, balloon flight trains experience a dynamic behavior typical of a floating multiple pendulum, which can be modeled with Lagrange's mechanics [13, 18] or multibody approaches [25, 26]. The validation of the dynamic model of the stratospheric balloon is rarely presented, since it requires to analyze the recorded data after the flight (the system being too large to be deployed in laboratory prior to the mission). In particular, let us note that spectral analysis is discussed in [2] for the FIREBall system, and in [27] for another balloon system called Apex; these data highlight strong resonances caused by the natural modes of the system, but they are not compared to theoretical dynamical models. A comparison between a dynamical model and recorded flight data is proposed in [26] for the BLAST system, but large discrepancies are observed on these natural frequencies, attributed to the parametric uncertainties in the system. To address these modeling issues, a complete dynamical model was proposed by the authors in [28] based on Lagrangian mechanics, to take into account the torsion and pendulum dynamics as well as their coupling. This model was compared to flight data and produced satisfying predictions of the dominant natural frequencies of the system. The first contribution of this paper is to complete this previous model with an empirical model of the frequency content of the wind disturbance, based on flight data, to match the power spectral density of the platform's motion.

Moreover, balloon systems involve uncertain or varying parameters. Indeed, the gondola generally carries ballast that initially represents a significant portion of the gondola's mass and that is released throughout the flight for altitude control, the balloon's properties (position of the center of buoyancy, moments of inertia, etc.) are difficult to predict and may vary during the flight, and more generally, experimental validation is rarely available since it requires to deploy the whole system in flight. In addition, it is often useful to be able to model and robustly assess the performance of the system as early as possible in the project's life, when the mechanical design, and the associated parameters (mass of the gondola, moments of inertia, etc.), are not yet precisely defined. The second contribution of this paper is a complete control-oriented model of the system which includes parametric uncertainties with the Linear Fractional Transformation (LFT) representation. This model is based on a multibody framework developed in [29]. The pointing system is also modeled, including line-of-sight estimation, sensors and actuators dynamics, and frequency content of the measurement noise. Such a model is adequate in the objective of an end-to-end process, allowing the control engineer to quickly take into account changes in the system's mechanical design, to compare different system or control architectures, robustly assess the performance in the early design phases, and progressively refine the model as the uncertainties get reduced during the design.

Once the dynamical model is obtained, it is possible to address the pointing control of the optical instrument onboard the gondola, generally a telescope [3, 5, 30–32] or siderostat [7, 33, 34]. However, in the literature, dynamical models of the balloon-borne system are rarely integrated in the control design. Instead, the control gains are generally tuned empirically based on ground testings [3, 30, 35–39], with simple control structures such as Proportional-Integral-Derivative (PID) gains [18, 32, 33, 40–42] possibly with some dynamic filters [2, 43, 44]. To the authors knowledge, there exists no general model-based methodology for controller synthesis in the literature, and, more critically, experimental ground-based setups are not representative of the dynamics of the fully deployed system in flight (which cannot be obtained in laboratory due to the dimensions of the system), whereas flight experience proves that the line-of-sight control is essentially limited by the rejection of the natural pendulum-like modes of the flight chain [2], excited by wind disturbance. Although some more advanced control techniques were investigated (pole assignment [2, 15], LQR synthesis [14], adaptive control [16], sliding mode control [21, 45], Lyapunov stability theory [26]), they provide very few insight on the achievable performance. The third contribution of this paper is a general methodology to address the line-of-sight pointing control of an optical instrument onboard a stratospheric balloon as a robust structured $\mathcal{H}_2/\mathcal{H}_\infty$ problem. Based on the LFT model presented in this paper and a non-smooth optimization algorithm [46–49] implemented in Matlab's robust control toolbox, it is shown how this framework takes full advantage of the knowledge of the system to improve the performance with regard to a traditional PID controller. This robust control synthesis is completed with a sensitivity analysis based on μ-analysis to identify the most impacting uncertain parameters, and provide formal lower and upper bounds of the robust performance.

Although the presented modeling and control methodology aim to have extent to stratospheric balloons in general, the paper relies on the case study of the Faint Intergalactic-medium Redshifted Emission Balloon (FIREBall), a joint NASA/CNES experiment. The modeling of the flight chain is described in Sect. 2. Then, Sect. 3 addresses the modeling of the pointing system. The robust control of the line-of-sight is performed in Sect. 4. Finally, the sensitivity of the pointing performance to the parametric uncertainties is examined in Sect. 5.

2 Modeling of the flight chain

2.1 The FIREBall flight chain

The stratospheric balloon FIREBall [7] is represented in Fig. 1. At the top of the flight chain, the balloon has a height of 120 m and is filled with helium. Just below the balloon is the un-deployed parachute, stored as a tube and integrated in the flight chain. Then, various elements such as bi-filar suspensions or rigid bodies are found. Finally, at the bottom of the flight chain, the gondola weights 1900 kg plus up to 500 kg of ballast (which can be released to control the altitude of the system, particularly during the day/night shift). Inside the gondola is the pointing system, which is detailed in Sect. 3. After lift-off, the system rises in about 3 h up to a relatively steady altitude around 39 km where the total and weight and buoyant forces compensate each other. The system follows the horizontal wind and undergoes some buoyant oscillations in altitude. A few hours are allocated for calibration and testing, and then ideally up to 8 h of science measurements. Finally, at the end of the mission, the balloon is teared up and detached from the rest of the system, the parachute is deployed, and the gondola is recovered on the ground.

The control architecture is the following: a primary control of the platform in azimuth (around the vertical axis **z**) is ensured by a motorized pivot, and reaction wheels additionally provide active damping to the pendulum-like oscillations (around **x** and **y**); the pointing system, in the platform, controls the line-of-sight to reject the remaining motion of the platform to achieve sub-arcsecond performance. This paper focuses on the modeling of the dynamics of the whole system during the pointing phase, and on the line-of-sight pointing control inside the platform. With this regard, the main challenge lies in the natural resonances of the system, excited by the wind disturbances and constituting the main contribution to the pointing error, as observed during the 2018 flight [2].

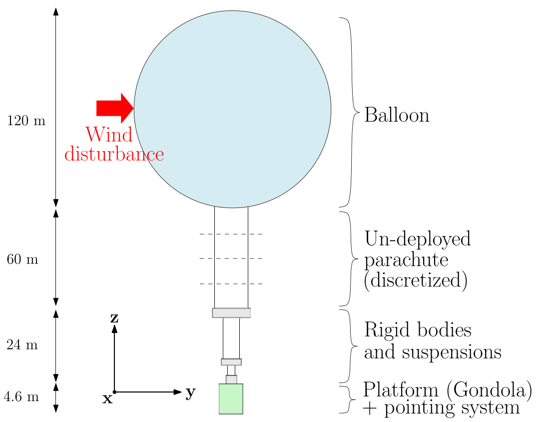

Fig. 1 Sketch of the FIREBall system (not in scale)

2.2 Nominal model with Lagrangian mechanics

A complete dynamical model of balloon-borne flight chains was proposed in [28] and applied to FIREBall. Generally speaking, the flight chain is considered to be composed of two types of bodies: rigid bodies (such as the platform) which can rotate in the three directions, and bi-filar suspensions, which are modeled as one single flexible body with a degree of freedom corresponding to their torsion around **z**. Note that the parachute is discretized and modeled as 4 bi-filar suspensions, and that the balloon is considered as a rigid body. The mechanisms between two successive bodies are revolute joints that allow the rotation around **x** and **y**. Two types of dynamics are distinguished: (i) the pendulum-like dynamics, corresponding to the oscillations of the elements of the flight chain around **x** and **y**, and (ii) the torsion dynamics, corresponding to the torsion of the bi-filar suspensions around the vertical axis **z**. With the small angles approximation, the pendulum and torsion dynamics are decoupled in open-loop, and the equations of motion are derived with Lagrangian mechanics:

$$\boldsymbol{\mu}\delta\ddot{\mathbf{X}} + \boldsymbol{\gamma}\delta\dot{\mathbf{X}} + \boldsymbol{\kappa}\delta\mathbf{X} = \delta\mathbf{T} \qquad (1)$$

where $\delta\mathbf{X}$ contains the degrees of freedom, $\delta\mathbf{T}$ is the vector of input forces and torques, the mass matrix $\boldsymbol{\mu}$ and the stiffness matrix $\boldsymbol{\kappa}$ are obtained following the method detailed in [28], and the damping matrix $\boldsymbol{\gamma}$ assumes natural dissipative effects in the rotation of the balloon and in the revolute joints. Since the values of the damping coefficients are not theoretically known, they were empirically estimated from flight data (see Sect. 2.3).

Remark: Despite only providing a nominal model without parametric uncertainties, Lagrangian mechanics provide a good first approach that requires less theoretical developments than the multibody approach that is presented in Sect. 2.4 *and has general extent to any balloon-borne flight chain.*

2.3 Disturbance model and validation based on flight data

The motion of the system is essentially caused by wind disturbances applied to the balloon. To reconstruct the frequency content of the gondola motion, given the model of the FIREBall system derived in Sect. 2.2, it now only remains to derive a model of the frequency content of the wind disturbance. This is done empirically based on flight data.

The wind disturbance is modeled as a colored noise acting on the linearized model of the flight chain. Let us note δF_y the force applied to the balloon's center of pressure along $\mathbf{y}$, and $D(s)$ the filter representing its frequency content:

$$\delta F_y(s) = D(s)\delta d_y(s) \tag{2}$$

where δd_y is a white noise input of unitary power spectral density (PSD): $\Phi_{\delta d_y}(j\omega) = 1$ where the function Φ_x designates the PSD of a signal x. From the nominal model presented in Eq. (1), let us note $G(s)$ the transfer function from δF_y to the platform's angle θ_x^p about $\mathbf{x}$. Assuming that the aerodynamic force is the sole contributor to the platform's oscillations, the PSD of θ_x^p reads:

$$\Phi_{\theta_x^p}(j\omega) = |D(j\omega)G(j\omega)|^2. \tag{3}$$

The function $D(s)$ was empirically determined to fit the general shape of the PSD $\Phi_{\theta_x^p}(j\omega)$ computed from flight data, meaning the offset at low frequencies (below 0.002 rad s^{-1}), the pole at 0.002 rad s^{-1}, and the zero at 0.15 rad s^{-1} with their associated damping coefficients:

$$D(s) = 4.62\frac{s^2 + 0.21s + 0.0225}{s^2 + 0.016s + 4 \times 10^{-4}}. \tag{4}$$

The result is shown in Fig. 2, with the PSD $\Phi_{\theta_x^p}(j\omega)$ computed from in-flight measurement (in blue), the theoretical model $|D(j\omega)G(j\omega)|^2$ (in red), and the PSD of the measurement noise (in grey dotted line). The damping coefficients in the matrix $\boldsymbol{\gamma}$ (see Sect. 2.2) were also adjusted to fit the amplitude of the resonances observed at 0.27 rad s^{-1}, 0.76 rad s^{-1}, 2.5 rad s^{-1} and 3.5 rad s^{-1} respectively, corresponding to the first four pendulum modes of the system. Modal dampings between 0.001 and 0.01 are obtained for these modes, as it can be expected for such flexible systems. The model fits up to 5 rad s^{-1}, in particular regarding these four natural frequencies (which only depend on the matrices $\boldsymbol{\mu}$ and $\boldsymbol{\kappa}$ in Eq. (1)). For higher frequencies, the signal is dominated by the measurement noise and no conclusion can be made. Nonetheless, as shown in Sect. 4, this frequency range is sufficient to validate the model for this application, since the control performance is determined by these four natural modes. The same filter $D(s)$ is used to model the aerodynamic force δF_x along $\mathbf{x}$.

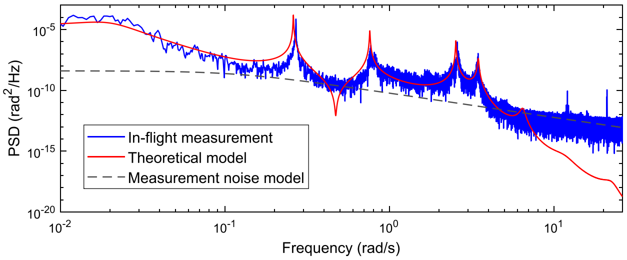

Fig. 2 Platform's motion frequency content: model VS flight data

Remark: the model $D(s)$ *obtained in Eq.* (4) *yields disturbances of higher amplitude than Dryden wind gusts models (with a factor* ~ 10), *which are widely used in aircraft design* [50, 51]. *It is suspected that the aerodynamic disturbances encountered during the balloon flight rather originate from the variations of the wind correlated with altitude oscillations* [52, 53]. *This is also suggested by the cutoff frequency of* $D(s)$ *that exactly coincides with the frequency of the buoyant oscillations. However, the model presented in this paper is purely empirical based on data of the FIREBall 2018 flight. A general disturbance model would most likely depend on the altitude of the mission and on the balloon properties.*

2.4 Uncertain LFT model with a multibody approach

2.4.1 Motivations

The nominal model in Sect. 2.2 along with the disturbance model in Sect. 2.3 yield a good prediction of the gondola's motion in terms of amplitude and frequency content in nominal conditions. However, it is valuable to account for parametric uncertainties which may modify the system's behavior. Indeed: (i) various parametric uncertainties may explain the small discrepancies between the model and the flight data in Fig. 2; in particular, the balloon's parameters are difficult to estimate and may vary during the flight (helium is released from the balloon's envelop), (ii) the ballast mass is initially 500 kg, but decreases down to 0 during the flight, (iii) more generally for balloon-borne experiments, flight data is not always available to validate the model, and the system cannot be deployed in laboratory for experimental validation prior to the mission due to its large dimensions, and (iv) some parameters, such as the gondola's mass or moments of inertia, might be subject to changes during the project's life, whereas it is necessary to assess the performance in the early design phases. Deriving a model which includes these parametric uncertainties then allows performing robust control and providing assessment of the pointing performance early in the design phase.

2.4.2 The LFT representation

The Linear Fractional Transformation (LFT) is chosen in this work for uncertainty representation. The LFT form allows representing the uncertain system with one single continuous model instead of a discrete family of parameterized models. It enables modern analysis and control tools such as the μ-analysis or the robust $\mathcal{H}_\infty$ control, to ensure robust stability and performance to parametric uncertainties.

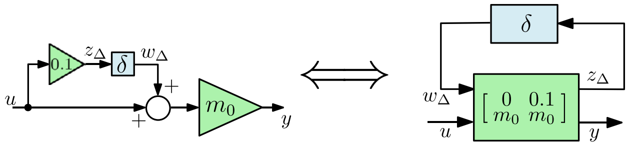

Fig. 3 Simple LFT representing an uncertain mass

For example, a mass m with ±10% of uncertainty can be represented as

$$m = m_0(1 + 0.1\delta) \tag{5}$$

where m_0 is the nominal value, and δ is an unknown real number verifying $|\delta| < 1$. Figure 3 shows the direct block diagram representation of Eq. (5) (left) and the equivalent LFT block diagram representation (right) where the uncertainty acts as a feedback on the nominal plant.

Generating a LFT model from the Lagrangian model from Eq. (1) is not a viable option since it yields many redundant occurrences of the uncertain parameters, which hinders the robust controller synthesis. Even though reduction methods exist, they will generally yield a larger number of repetitions than a method that is directly minimal or close to minimality. Therefore, a general approach was developed in [29] to compute LFT models of multibody systems, such as stratospheric balloons in this paper. In this approach, each substructure (body, kinematic joint, etc.) has its individual LFT model based on Newton–Euler equations, expressing the relationship between the motion of the substructure and the wrench (force and torque) applied to it. These individual models are then assembled to build the complex multibody structure while taking care of the dependency of the trim conditions to the uncertain parameters. The LFT model of the structure is finally obtained as a continuous function of the uncertain parameters, with a limited (although non-minimal) number of occurrences, and covers all plants within the specified bounds in a single model, without introducing conservatism or gridding error.

2.4.3 Application to FIREBall

Following the method presented in [29], the LFT model of a multibody structure, such as the FIREBall system, can be assembled as follows.

Individual model of each substructure composing the system:

Considering the linear dynamics around the equilibrium, let us call "wrench" the vector $\delta\mathbf{W}_{\mathcal{A}/\mathcal{B},P} \in \mathbb{R}^6$ containing the force and torque applied by a body $\mathcal{A}$ to a body $\mathcal{B}$ at point P, and "motion vector" the vector $\delta\mathbf{m}_P^{\mathcal{B}} \in \mathbb{R}^{18}$ containing the linear and angular accelerations, speeds and positions of body $\mathcal{B}$ at point P. The generic linearized models of the bodies (rigid bodies, bi-filar suspensions and revolute joints) constituting the FIREBall system are represented in Fig. 4:

- In the forward dynamics model of a rigid body (Fig. 4a), the inputs are the wrenches $\delta\mathbf{W}_{./\mathcal{B},P_1}$ and $\delta\mathbf{W}_{./\mathcal{B},P_2}$ applied to $\mathcal{B}$ at connection points P_1 and P_2. The model returns the motion vectors $\delta\mathbf{m}_{P_1}^{\mathcal{B}}$ and $\delta\mathbf{m}_{P_2}^{\mathcal{B}}$ at the connection points P_1 and P_2. The forward dynamics model is a 12th-order dynamical model (the wrenches are integrated twice to produce the motion vector).
- In the inverse dynamics model of a rigid body (Fig. 4b), the motion vector $\delta\mathbf{m}_{P_1}^{\mathcal{B}}$ is imposed as input at one connection point P_1, and a wrench $\delta\mathbf{W}_{./\mathcal{B},P_2}$ is applied at point P_2. The model returns the wrench $\delta\mathbf{W}_{\mathcal{B}/.,P_1}$ applied by the body in reaction at P_1 and the motion vector $\delta\mathbf{m}_{P_2}^{\mathcal{B}}$ at P_2. The inverse dynamics model is a static model.
- The model of the bi-filar suspension (Fig. 4c) has the same inputs and outputs as the inverse dynamics model of a rigid body. However, the bi-filar suspension model has an additional degree of freedom corresponding to the twist around the vertical axis (see [28] for the bi-filar suspension model based on Lagrangian mechanics). It is a 2nd-order dynamic model.
- The revolute joint connects two given bodies noted $\mathcal{A}$ and $\mathcal{B}$ at connection point P with a degree of freedom in rotation. It is a 2nd-order dynamic model.

Each nominal model (green blocks) is augmented as an LFT model with parametric uncertainties, represented by the unknown, bounded operators $\mathbf{\Delta}_{(.)}$ (blue blocks). In particular, the blocks $\mathbf{\Delta}_{\mathcal{J}}$ in the revolute joints correspond to uncertainties in the stiffness due to uncertain masses in the flight chain. The reader is referred to [29] for more details on the derivation of these individual linearized models, based on Newton–Euler equations.

Assembly of the multibody structure:

The individual substructure models are assembled following the procedure presented in [29] to build the model of the FIREBall system represented in Fig. 1. The linearized model

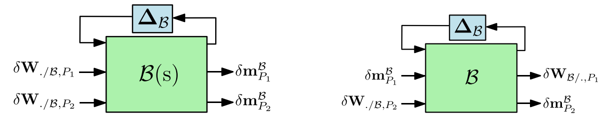

(a) Rigid body (forward dynamics) (b) Rigid body (inverse dynamics)

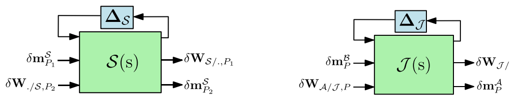

(c) Bi-filar suspension (d) Revolute joint

Fig. 4 Individual models constituting the balloon system of the flight chain, composed of 5 rigid bodies (the balloon is modeled with a forward dynamics model, and all other rigid bodies with an inverse dynamics model), 6 bi-filar suspensions (including 4 to model the discretized parachute), and 10 joints (at connection points P_1 to P_{10}), is represented in Fig. 5. The joints $\mathcal{J}_1$ to $\mathcal{J}_9$ allow the rotation around $\mathbf{x}$ and $\mathbf{y}$.

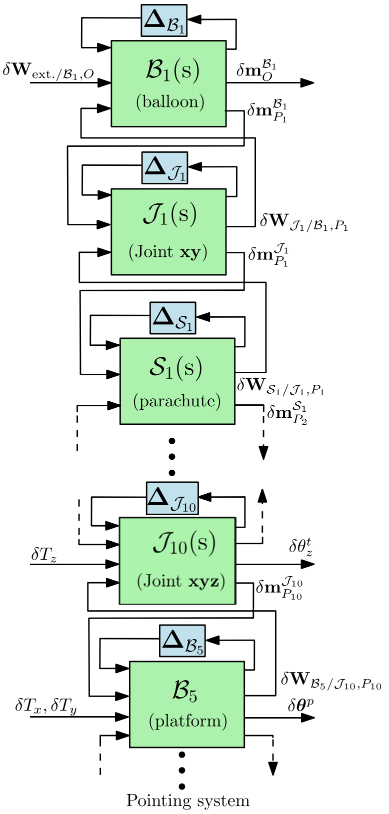

Fig. 5 Multibody LFT model of the flight chain

$\mathcal{J}_{10}$ can additionally be actuated by a torque δT_z around the vertical axis $\mathbf{z}$ to model the azimuth control, and the torques δT_x and δT_y can be applied to the platform using reaction wheels (see Sect. 2.5). The output vector $\delta\boldsymbol{\theta}^p$ contains the 3 angles of the platform, and the output scalar $\delta\theta_z^t$ is the flight train's angle around $\mathbf{z}$. The input $\delta\mathbf{W}_{\text{ext.}/\mathcal{B}_1,O}$ contains the aerodynamic disturbances (input), the damping terms (added as feedback on the rotation rates of the balloon), and the variations of the buoyancy force projected in the reference frame attached to the balloon (added as feedback on the angular position of the balloon).

Two types of parametric uncertainties are considered:

- the uncertainties related to the early phases of the design, when the mechanical design is not yet fixed, related to the gondola: moments of inertia (in addition to the main moments of inertia, the matrix of inertia has coupling terms between the x and z axes; each of these moments of inertia has ±5% of uncertainty), mass (±5%), center of mass (±0.1m);
- the uncertainties that are inherent to the system: (i) ballast mass (comprised between 0 and 500 kg), (ii) balloon's parameters: main moments of inertia (±5%), mass (±5%), center of pressure (±3 m), center of mass (±3 m), center of buoyancy (±3 m).

After implementation on MATLAB, the total number of occurrences of the uncertain parameters is 89, and the model has order 66. It is verified that the nominal realization of this uncertain model exactly matches the nominal model obtained in Sect. 2.2. The uncertain transfer between a wind disturbance and the gondola's angle is represented in Fig. 6 with 500 samples randomly selected across the parametric space using Matlab's routine usample. The impact of the

Fig. 6 Transfer: wind to platform's angle (500 samples)

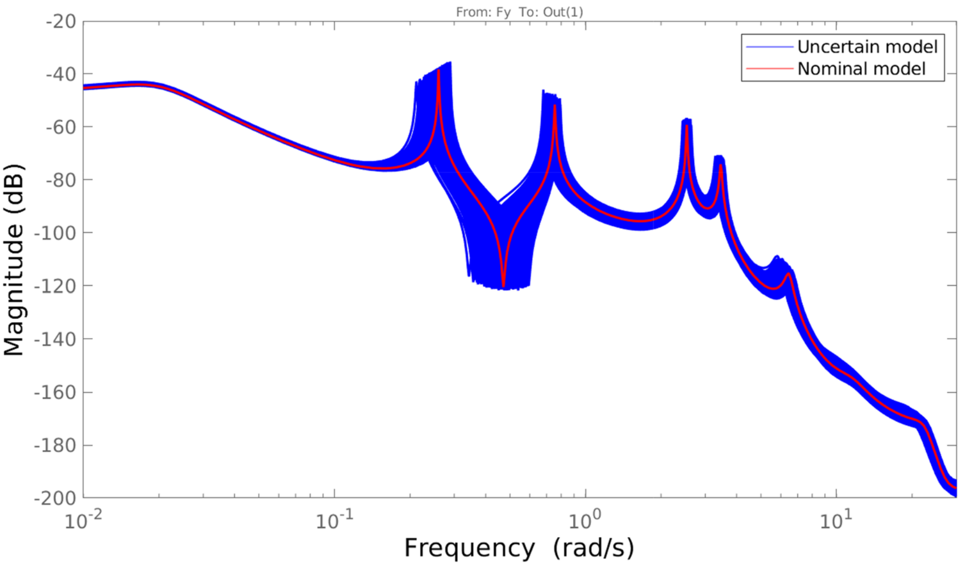

parametric uncertainties on the response of the system to wind disturbance, and in particular on the natural frequencies of the system, can clearly be seen.

2.5 Primary control of the platform

The primary control ensures that the azimuth of the platform (angle around the vertical axis **z**) follows the sideral motion of the target. It is only briefly summarized here, because the associated pointing requirements are not very demanding, and because the possible destabilizing effect of the azimuth control on the flight chain was specifically addressed in [28].

The primary control in azimuth is performed with a motorized pivot, which applies a torque δT_z to the gondola and the opposite torque $-\delta T_z$ to the bottom of the flight chain. The torque is computed with two 2nd-order controllers $C_1(s)$ and $C_2(s)$ using the reference azimuth δr_{az}, the estimated platform's angle $\delta\theta_z^p$ and the estimated flight train's angle $\delta\theta_z^t$:

$$\delta T_z = C_1(s)(\delta r_{az} - \delta\hat{\theta}_z^p) + C_2(s)\delta\hat{\theta}_z^t \tag{6}$$

with the estimated angles

$$\begin{cases} \delta\hat{\theta}_z^p = d(s)\delta\theta_z^p \\ \delta\hat{\theta}_z^t = d(s)\left(\frac{40s}{40s+1}\right)^2\delta\theta_z^t \end{cases} \tag{7}$$

where $d(s)$ designates a third-order Padé approximation of a 70 ms delay, and a low-pass filter is applied to the flight train's angle $\delta\theta_z^t$ (to avoid low-frequency drift, and because only the platform should be controlled in low-frequency). The flight train's angle is measured by a tachometer inside the motorized pivot, and the platform's angle is provided by a 3-axes Inertial Measurement Unit (IMU) using accelerometers and fiber-optic gyroscopes; more information on the hardware of the FIREBall system is available in [2, 43]. The controllers

$$\begin{cases} C_1(s) = \frac{3043s^2+958000s+7360}{s^2+357s+900} \\ C_2(s) = \frac{140s^2+3259s+166}{s^2+357s+900} \end{cases} \tag{8}$$

were tuned so as to provide a 1 rad s^{-1} control bandwidth while stabilizing the torsion modes of the flight train, using a similar $\mathcal{H}_\infty$ synthesis as presented in this paper for the line-of-sight control.

In addition to the azimuth control, the FIREBall system carries two reaction wheels able to generate a torque about **x** and **y** respectively. Taking the rotation rates of the platform $\delta\dot{\theta}_x^p$ and $\delta\dot{\theta}_y^p$ as inputs, the controller $C_3(s)$ is tuned to provide active damping to the pendulum modes 3 and 4, because they play an important role in the pointing performance [2]. The torques generated by the wheel read:

$$\begin{bmatrix} \delta T_x \\ \delta T_y \end{bmatrix} = -\underbrace{\frac{0.885s}{s+1.847}}_{\text{Actuator model}}\ \underbrace{\frac{1233s+963}{s^2+0.76s+6.3}}_{C_3(s)}\,d(s)\begin{bmatrix} \delta\dot{\theta}_x^p \\ \delta\dot{\theta}_y^p \end{bmatrix}. \tag{9}$$

3 Modeling of the pointing system

The purpose of the pointing system is to reject the gondola's motion (up to 0.15° of amplitude [2]), after the primary control ensured by the reaction wheels and motorized pivot, to obtain a line-of-sight pointing accuracy around the arc second (elevation and cross-elevation axes) and arc minute (field rotation axis).

3.1 Description of the pointing system

The pointing system is represented in Fig. 7. The siderostat mirror is mounted on a gimbal equipped with two DC motors which allow it to be controlled around two axes called elevation and cross-elevation. The light is reflected on the siderostat mirror, and then concentrated by a parabolic mirror to the instrument through a hole in the siderostat mirror. The instrument is mounted on a rotating stage, allowing a third axis called field rotation to be controlled. Let us note $\mathcal{R}_1 = (\mathbf{x}_1, \mathbf{y}_1, \mathbf{z}_1)$ the reference frame attached to the platform (gondola). The line-of-sight, represented with the frame $\mathcal{R}_4 = (\mathbf{x}_4, \mathbf{y}_4, \mathbf{z}_4)$, is defined with the three successive rotations:

- A first rotation around $\mathbf{y}_1$ defines the frame $\mathcal{R}_2 = (\mathbf{x}_2, \mathbf{y}_2, \mathbf{z}_2)$. The angle between $\mathcal{R}_1$ and $\mathcal{R}_2$ is called elevation and equals $10° + 2\theta_{\text{el}}$, where θ_{el} is the angle of the siderostat mirror around $\mathbf{y}_1$. The factor 2 is due to the reflection of the light on the siderostat mirror, and the term 10° is due to the angular position of the parabolic mirror.

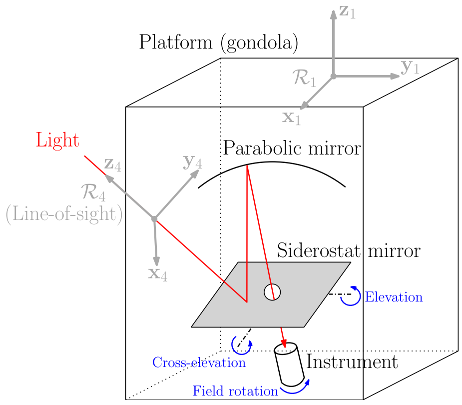

Fig. 7 Sketch of the pointing system

- A second rotation around $\mathbf{x}_2$ defines the frame $\mathcal{R}_3 = (\mathbf{x}_3, \mathbf{y}_3, \mathbf{z}_3)$. The angle between $\mathcal{R}_2$ and $\mathcal{R}_3$ is called cross-elevation and equals $2\theta_{\mathrm{ce}}$, where θ_{ce} is the angle of the siderostat mirror around $\mathbf{x}_2$. The factor 2 is due to the reflection of the light on the siderostat mirror.
- A third rotation around $\mathbf{z}_3$ defines the frame $\mathcal{R}_4 = (\mathbf{x}_4, \mathbf{y}_4, \mathbf{z}_4)$ attached to the line-of-sight. The angle between $\mathcal{R}_3$ and $\mathcal{R}_4$ is called field rotation and is noted θ_{fr}.

3.2 Definition of the line-of-sight

Let us note $\boldsymbol{\theta}^{\mathrm{EUL}}$ the vector containing the Euler angles (in any given sequence) defining the orientation of $\mathcal{R}_4$ with regard to an inertial frame. It can be expressed as a function of the vector $\boldsymbol{\theta}^{p}$ containing the Euler angles of the platform, and of the vector $\boldsymbol{\theta}^{a} = \begin{bmatrix}\theta_{\mathrm{el}} & \theta_{\mathrm{ce}} & \theta_{\mathrm{fr}}\end{bmatrix}^{\mathrm{T}}$ containing the angles of the three rotations imposed by the actuators (elevation, cross-elevation, field rotation) to the mirror or instrument. To the first order, this relationship reads:

$$\delta\boldsymbol{\theta}^{\mathrm{EUL}} = \left.\frac{\partial\boldsymbol{\theta}^{\mathrm{EUL}}}{\partial\boldsymbol{\theta}^{p}}\right|_{\mathrm{eq}} \delta\boldsymbol{\theta}^{p} + \left.\frac{\partial\boldsymbol{\theta}^{\mathrm{EUL}}}{\partial\boldsymbol{\theta}^{a}}\right|_{\mathrm{eq}} \mathbf{R}\delta\boldsymbol{\theta}^{a} \tag{10}$$

where the matrix $\mathbf{R} = \operatorname{diag}(2, 2, 1)$ accounts for the reflections on the elevation and cross-elevation axes, and the 3×3 matrices $\frac{\partial\boldsymbol{\theta}^{\mathrm{EUL}}}{\partial\boldsymbol{\theta}^{p}}$ and $\frac{\partial\boldsymbol{\theta}^{\mathrm{EUL}}}{\partial\boldsymbol{\theta}^{a}}$ account for the rotations. At equilibrium, the actuator's elevation angle $\bar{\theta}_{\mathrm{el}}$ is comprised between 5° and 20°, corresponding to a LOS elevation angle comprised between 20° and 50° (as defined in Sect. 3.1), and the cross-elevation and field rotation angles are zero. It is important to account for the different values that the equilibrium elevation angle $\bar{\theta}_{\mathrm{el}}$ can have during the flight, since it changes the influence of the platform's motion, and consequently of the wind disturbance, on the cross-elevation and field rotation axes. Therefore, $\bar{\theta}_{\mathrm{el}}$ is considered as an uncertain parameter in this study. As discussed in [54, p. 191 to 195], it is necessary to define the uncertain parameter $t_{\mathrm{el}} = \tan(\bar{\theta}_{\mathrm{el}}/2)$, instead of $\bar{\theta}_{\mathrm{el}}$, in the LFT representation, because the sine and cosine functions can be expressed as rational expressions in the variable t_{el}.

Provided that $\frac{\partial\boldsymbol{\theta}^{\mathrm{EUL}}}{\partial\boldsymbol{\theta}^{a}}$ is invertible, let us define the new vector $\delta\boldsymbol{\theta}^{\mathrm{LOS}}$ describing the motion of the line-of-sight in terms of elevation, cross-elevation and field rotation, such that

$$\delta\boldsymbol{\theta}^{\mathrm{LOS}} = \left.\frac{\partial\boldsymbol{\theta}^{\mathrm{EUL}}}{\partial\boldsymbol{\theta}^{a}}\right|_{\mathrm{eq}}^{-1} \delta\boldsymbol{\theta}^{\mathrm{EUL}} = \underbrace{\left.\frac{\partial\boldsymbol{\theta}^{\mathrm{EUL}}}{\partial\boldsymbol{\theta}^{a}}\right|_{\mathrm{eq}}^{-1} \left.\frac{\partial\boldsymbol{\theta}^{\mathrm{EUL}}}{\partial\boldsymbol{\theta}^{p}}\right|_{\mathrm{eq}}}_{=\mathbf{P}(t_{\mathrm{el}})=\mathcal{F}_u(\mathbf{P},\boldsymbol{\Delta}_{t_{\mathrm{el}}})} \delta\boldsymbol{\theta}^{p} + \mathbf{R}\delta\boldsymbol{\theta}^{a}. \tag{11}$$

The vector $\delta\boldsymbol{\theta}^{\mathrm{LOS}}$ is introduced because (i) the science requirements and the levels of noise of the optical sensor are expressed with this convention, and (ii) the action of the actuators on the line-of-sight angles are decoupled in Eq. (11) (the matrix $\mathbf{R}$ is diagonal) which facilitates the controller design. The matrix $\mathbf{P}(t_{\mathrm{el}})$ expresses the relation between the gondola's motion and the LOS depending on t_{el}, and is expressed as the LFT $\mathcal{F}_u(\mathbf{P}, \boldsymbol{\Delta}_{t_{\mathrm{el}}})$, where $\mathcal{F}_u(.)$ designates the upper LFT operator.

3.3 Estimation of the line-of-sight

Three sets of sensors are used to estimate the line-of-sight:

- An optical sensor is attached to the instrument and provides a direct measurement of the line-of-sight, noted $\widehat{\delta\boldsymbol{\theta}}^{\mathrm{LOS}}_{\mathrm{optic}}$. It has low noise (around ± 0.1 arcsec in elevation and cross-elevation, $\pm$ 10 arcsec in field rotation, sampled at 30 Hz) but has an uncertain delay t_o of 30–40 ms, due to the exposure time of the sensor and some processing delays, which limits the closed-loop performance and stability.
- Another estimate, noted $\widehat{\delta\boldsymbol{\theta}}^{\mathrm{LOS}}_{\mathrm{gyro}}$, is calculated with Eq. (11) from the two measurements:
  - Analogical gyrometers deliver the rotation rates of the platform with high noise (around $\pm$ 20 arcsec/s at 200 Hz) but no delay. These rotation rates are integrated to get an estimate $\widehat{\delta\boldsymbol{\theta}}^{p}$ of the attitude of the gondola.
  - The position of each actuator is measured relatively to the gondola with negligible noise (with regard to the attitude provided by the gyrometers). The delay of this measurement is taken into account in the actuators model in Sect. 3.4. This measurement is noted $\widehat{\delta\boldsymbol{\theta}}^{a}$.
  - The estimate then reads: $\widehat{\delta\boldsymbol{\theta}}^{\mathrm{LOS}}_{\mathrm{gyro}} = \mathbf{P}(t_{\mathrm{el}})\widehat{\delta\boldsymbol{\theta}}^{p} + \mathbf{R}\widehat{\delta\boldsymbol{\theta}}^{a}$.

The line-of-sight measured by the optical sensor $\widehat{\delta\boldsymbol{\theta}}^{\mathrm{LOS}}_{\mathrm{optic}}$ provides a good estimate at low frequencies, but cannot be used in high frequencies due to the 40 ms delay. On the contrary, the gyrometers/actuators estimation $\widehat{\delta\boldsymbol{\theta}}^{\mathrm{LOS}}_{\mathrm{gyro}}$ cannot be used in low frequencies due to the integration of the rate measurement resulting in high noise levels. Therefore, the optical sensor and the gyrometers/actuators measurements are filtered to provide an estimate $\widehat{\delta\boldsymbol{\theta}}^{\mathrm{LOS}}$:

$$\widehat{\delta\boldsymbol{\theta}}^{\mathrm{LOS}} = \left(\mathbf{I}_3 - \mathbf{F}(\tau_1, \tau_2, s)\right)\widehat{\delta\boldsymbol{\theta}}^{\mathrm{LOS}}_{\mathrm{optic}} + \mathbf{F}(\tau_1, \tau_2, s)\widehat{\delta\boldsymbol{\theta}}^{\mathrm{LOS}}_{\mathrm{gyro}} \tag{12}$$

where the high-pass filter $\mathbf{F}(\tau_1, \tau_2, s)$ is expressed as a LFT with two parameters τ_1 and τ_2 ($\mathcal{F}_l(.)$ designates the lower LFT operator):

$$\begin{aligned}\mathbf{F}(\tau_1,\tau_2,s) &= \frac{\tau_1 s}{\tau_1 s+1}\frac{\tau_2 s}{\tau_2 s+1}\mathbf{I}_3\\ &= \mathcal{F}_l\left(\mathbf{F}(s), \begin{bmatrix}\tau_1\mathbf{I}_3 & \mathbf{0}\\ \mathbf{0} & \tau_2\mathbf{I}_3\end{bmatrix}\right).\end{aligned} \tag{13}$$

The structure of the filter presented in Eq. (13) was fixed for the mission. It corresponds to a classical gyro-stellar hybridization using a complementary filter; essentially, the idea is to rely on the optical measurements in low frequencies, and on the gyrometer measurements in high frequencies. It is composed of two first-order filters, whose two parameters τ_1 and τ_2 can be tuned to address the trade-off between noise levels, stability and rejection of the wind disturbance. This trade-off is coupled with the controller synthesis. Therefore, the parameters τ_1 and τ_2 will be tuned simultaneously with the controller. The values $\tau_1 = 0.1$ s and $\tau_2 = 0.5$ s were used during FIREBall 2018 flight.

The block diagram in Fig. 8 represents the sensors model and the estimation described in this section and implemented for controller synthesis. The transfer function of the uncertain optical measurement delay t_o is treated as 3rd-order Padé approximation noted $D_{\text{optic}}(s, t_o)$:

$$\begin{aligned}D_{\text{optic}}(s,t_o) &= \frac{-s^3+(12/t_o)s^2-(60/t_o^2)s+(120/t_o^3)}{s^3+(12/t_o)s^2+(60/t_o^2)s+(120/t_o^3)}\\ &= \mathcal{F}_u(D_{\text{optic}}(s), \mathbf{\Delta}_{t_o}).\end{aligned} \tag{14}$$

The measurement noise of the optical sensor is treated as a white noise in the frequency range 0–30 Hz; the measurement noise of the gyrometer is treated as a white noise in the frequency range 0–200 Hz, which is integrated to provide the position. The inputs $\delta\mathbf{n}_{\text{gyro}}$ and $\delta\mathbf{n}_{\text{optic}}$ are white Gaussian noises with unitary power spectral density; the filters modeling the noise frequency contents are

$$\begin{cases}\mathbf{W}_n^{\text{gyro}} = 5\times10^{-6}\frac{\mathbf{I}_3}{s} & (\text{rad/s}/\sqrt{\text{Hz}})\\ \mathbf{W}_n^{\text{optic}} = 4.5\times10^{-8}\,\text{diag}\,(1,1,100) & (\text{rad}/\sqrt{\text{Hz}})\end{cases}. \tag{15}$$

3.4 Actuation system

A revolute joint is used to model each rotation mechanism of the mirror or instrument. Contrary to the revolute joints used in the modeling of the flight chain (see Fig. 4d in Sect. 2.4), each revolute joint used in the pointing system is actuated. It takes the angular acceleration $\delta\ddot{\theta}$ imposed by the actuator between the two bodies designated with the generic notations $\mathcal{A}$ and $\mathcal{B}$. The angular configuration $\delta\theta$ is returned as output. For example, the elevation mechanism is represented in Fig. 9. The nominal model of the joint is noted $\mathcal{J}_{\text{el}}$, and the block $\mathbf{\Delta}_{t_{\text{el}}}$ represents the uncertainties due to the elevation angle at equilibrium $\bar{\theta}_{\text{el}}$. Each actuator is represented by a first-order transfer function between the input voltage δV_{el} and the angular acceleration imposed to the mirror or instrument (Table 1), resulting from a low-level control loop that is not designed here. An uncertain

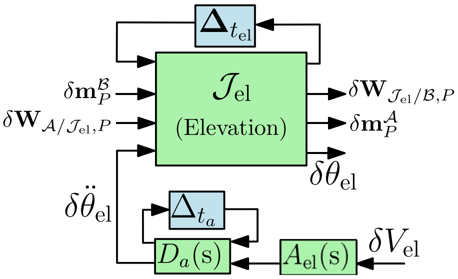

Fig. 9 Elevation actuation system

Fig. 8 Line-of-sight estimation

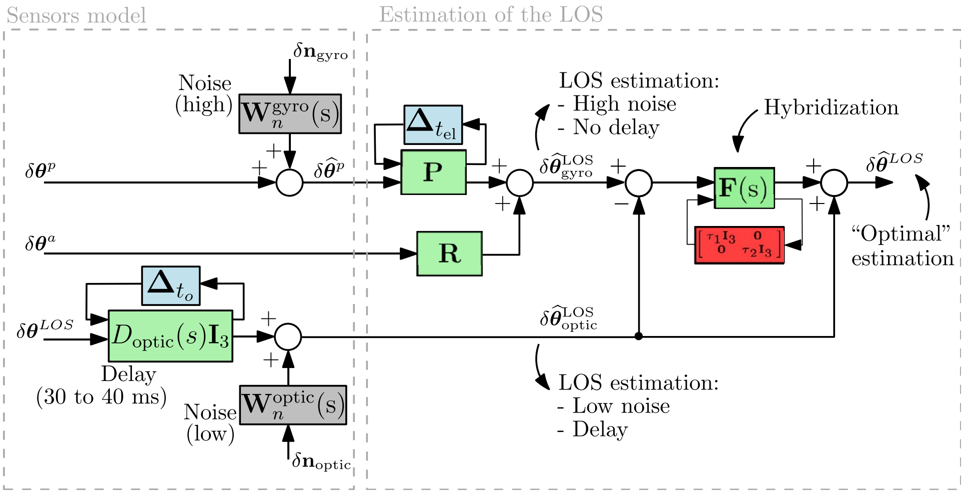

delay of 0.5–1 ms is also modeled on each actuator with a 3rd-order Padé's approximation noted $\mathcal{F}_u(D_a(s), \mathbf{\Delta}_{t_a})$.

Finally, the pointing system is represented in Fig. 10. The mirror is a rigid body with a matrix of inertia $\mathbf{J} = \mathrm{diag}\,(30, 30, 50)\,\mathbf{I}_3$ kg m^2. Note that its mass was already taken into account in the mechanical model of the gondola, since it influences its total mass, moments of inertia and position of its center of mass. The inertia of the instrument in field rotation is negligible, and thus it is not represented. The interconnection signals are not named for readability—see Fig. 9 for the details on a single axis actuation system. The input voltages are noted δV_{el}, δV_{ce} and δV_{fr} for the elevation, cross-elevation and field rotation actuators respectively. The outputs of the system are the angle of each actuator, respectively $\delta\theta_{\mathrm{el}}$, $\delta\theta_{\mathrm{ce}}$ and $\delta\theta_{\mathrm{fr}}$, and the line-of-sight angles $\delta\boldsymbol{\theta}^{\mathrm{LOS}}$.

3.5 Controller

An initial controller $\mathbf{K}_0(s)$ is proposed before the robust synthesis. The controller takes the estimated pointing error as input, and generates the voltage to be sent to the actuators; it is composed of three independent controllers in elevation, cross-elevation, and field rotation, as justified by Eq. (11), and tuned with a pole placement method:

$$\mathbf{K}_0(s) : \begin{cases} K_0^{\mathrm{el}}(s) = \frac{1}{2}\frac{1.7e{-6}}{0.01s+1}(K_p + K_d s)F(s) \\ K_0^{\mathrm{ce}}(s) = \frac{1}{2}\frac{3.81e{-6}}{0.01s+1}(K_p + K_d s)F(s) \\ K_0^{\mathrm{fr}}(s) = \frac{5e{-5}}{0.01s+1}(K'_p + K'_d s)F(s) \end{cases} \tag{16}$$

where:

- $K_p = \omega_0^2$, $K_d = 2\xi\omega_0$ with $\xi = 1$ and $\omega_0 = 50\,\mathrm{rad\,s^{-1}}$, and $K'_p = \omega_0'^2$, $K'_d = 2\xi\omega'_0$ with $\omega'_0 = 10\,\mathrm{rad\,s^{-1}}$, allow approximately placing the closed-loop poles,
- the factors 1/2 compensate for the factor 2 due to the reflection on the mirror on the elevation and cross-elevation axes,
- the factors 1.7e−6, 3.81e−6 and 5e−5 correspond to the inverse high-frequency gain of the actuators transfer functions,
- the low-pass filters $\frac{1}{0.01s+1}$ and the anti-aliasing filter $F(s)$ cut high frequencies, with $T_s = 0.02$ s:

$$F(s) = \frac{\pi^2}{T_s^2 s^2 + 1.4\pi T_s s + \pi^2}. \tag{17}$$

Although this controller is not exactly the one that was used in the FIREBall flight in 2018, it was tuned in a similar fashion so as to provide a similar control bandwidth. Moreover, it yields a good order of magnitude of the pointing performance. Figure 11 shows the pointing error in elevation and cross-elevation (top plot) and the actuators motion (bottom plot) in response to the wind disturbance, modeled as the colored noise presented in Sect. 2.3. This simulation can be compared to the flight data presented in [2], in particular regarding three aspects: (i) the pointing error is around the arcsecond, (ii) the error on the cross-elevation axis is slightly higher than on the elevation axis, (iii) the low-frequency

Table 1 Transfer functions of the actuators

Elevation	Cross-elevation	Field rotation
$A_{\mathrm{el}}(s) = 18800\frac{s}{0.032s+1}$	$A_{\mathrm{ce}}(s) = 4200\frac{s}{0.016s+1}$	$A_{\mathrm{fr}}(s) = 1000\frac{s}{0.050s+1}$

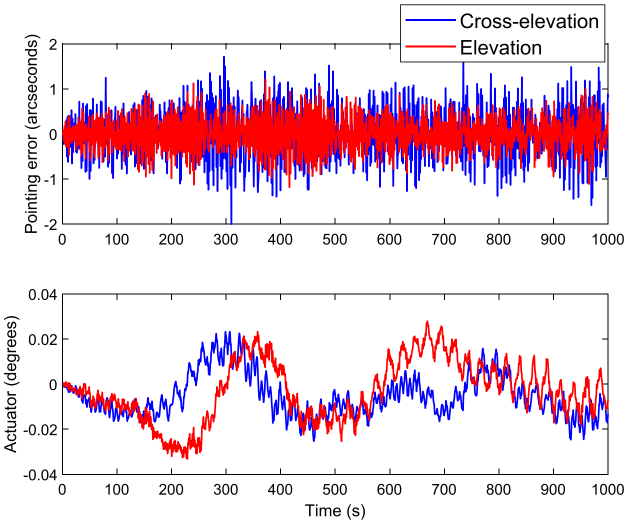

Fig. 11 Simulation: response to a colored noise wind disturbance

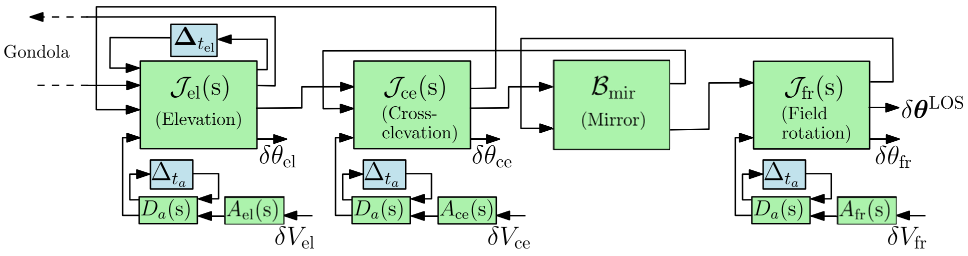

Fig. 10 3-axes pointing system

motion of the gondola is very efficiently rejected by the actuators (bottom plot), such that only higher frequency content remains on the pointing error (top plot).

Remark: *This initial controller does not exploit much of the available model information (natural frequencies of the flight chain, noise models, sensors delays, parametric uncertainties, etc.). The goal of the methodology presented in this paper is to take advantage of the proposed model to improve the pointing performance, in particular with regard to the rejection of the wind disturbance, using a model- and optimization-based method based on the* $\mathcal{H}_\infty$ *synthesis.*

4 Robust control of the line-of-sight

4.1 Theoretical elements

In this paper, the pointing control of the line-of-sight onboard the stratospheric balloon is formulated as a robust structured $\mathcal{H}_2/\mathcal{H}_\infty$ problem. The main theoretical elements are briefly recalled here.

The $\mathcal{H}_2$ and $\mathcal{H}_\infty$ norms

Consider a transfer matrix $\mathbf{G}(s)$ such that $\mathbf{y}(s) = \mathbf{G}(s)\mathbf{u}(s)$. The $\mathcal{H}_\infty$ norm is induced by the $\mathcal{L}_2$ norm:

$$\|\mathbf{G}(s)\|_\infty = \sup_{\mathbf{u}\neq\mathbf{0}} \frac{\|\mathbf{y}\|_2}{\|\mathbf{u}\|_2} = \sup_{\omega} \sigma_{\max}(\mathbf{G}(j\omega)) \tag{18}$$

and can therefore be equivalently interpreted as the maximum amplification factor of the signal energy from input to output, which makes it useful for evaluating performance in a control problem, or as the maximum singular value ($\sigma_{\max}$) over all frequencies (which can easily be read on a Bode diagram).

The $\mathcal{H}_2$ norm can also be defined:

$$\|\mathbf{G}(s)\|_2^2 = \frac{1}{2\pi}\int_{-\infty}^{+\infty} \mathrm{Tr}(\mathbf{G}^{\mathrm{T}}(-j\omega)\mathbf{G}(j\omega))\mathrm{d}\omega \tag{19}$$

to measure the variance of the output signal $\mathbf{y}$ when the input $\mathbf{u}$ is a white noise with unitary power spectral density.

Robust structured $\mathcal{H}_\infty$ control

Consider the standard closed-loop model represented in Fig. 12 with a plant $\mathbf{M}(s)$, a controller $\mathbf{K}(s)$ to be tuned, and parametric uncertainties represented by the block $\boldsymbol{\Delta}\in\mathbb{D}$ where $\mathbb{D}$ is the set of all possible parametric configurations.

The robust structured $\mathcal{H}_\infty$ control problem [48] consists in computing an optimal controller $\mathbf{K}^*(s)\in\mathcal{K}$ which stabilizes the plant in all parametric configurations, and which minimizes the $\mathcal{H}_\infty$ norm of the transfer between $\mathbf{w}$ and $\mathbf{z}$ with regard to the worst-case configuration:

Fig. 12 Standard closed-loop model

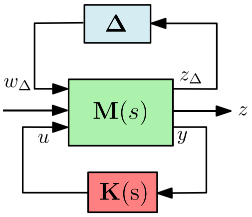

$$\begin{aligned}&\underset{\mathbf{K}(s)\in\mathcal{K}}{\text{minimize}}\ \max_{\boldsymbol{\Delta}\in\mathbb{D}} \|\mathcal{F}_l(\mathcal{F}_u(\mathbf{M},\boldsymbol{\Delta}),\mathbf{K})\|_\infty\\ &\text{such that } \mathbf{K}(s) \text{ stabilizes } \mathcal{F}_u(\mathbf{M},\boldsymbol{\Delta}) \text{ for all } \boldsymbol{\Delta}\in\mathbb{D}\end{aligned} \tag{20}$$

where $F_l(.)$ and $F_u(.)$ denote respectively the lower and upper LFT, and $\mathcal{K}$ denotes the space of the controllers of the desired structure: e.g., of reduced order, PID, observed-based, etc. Even in the case without parametric uncertainty ($\boldsymbol{\Delta}=\mathbf{0}$), this problem is non-convex (it is only convex in the unstructured case, i.e., if $\mathcal{K}$ contains all controllers of the same order as $\mathbf{M}(s)$ without any imposed structure), and the non-smooth optimization algorithm implemented in the SYSTUNE routine of MATLAB provides a locally optimal solution, even for large size problems [46]. This formulation also handles constraints based on the $\mathcal{H}_2$ norm, and multi-objective problems [49]. Finally, this algorithm addresses the problem with parametric uncertainties ($\boldsymbol{\Delta}\neq\mathbf{0}$) through a heuristic search of worst-case configurations [47].

4.2 Closed-loop model

Based on the modeling presented in Sects. 2 and 3, the closed-loop system, of order 152 with 135 repetitions of the uncertain parameters, is represented in Fig. 13:

- The green blocks represent the nominal system: $\mathbf{M}(s)$ includes the flight chain, $\mathbf{E}(s)$ represents the estimation (Sect. 3.3), and $\mathbf{A}(s)$ regroups the actuators dynamics (Sect. 3.4),
- The blue blocks $\boldsymbol{\Delta}_M$, $\boldsymbol{\Delta}_E$ and $\boldsymbol{\Delta}_A$ regroup the parametric uncertainties discussed earlier on the mechanical system, estimation and actuators' models respectively,
- The red blocks are the tuning parameters: controller $\mathbf{K}(s) = \mathrm{diag}\left(K^{\mathrm{el}}(s), K^{\mathrm{ce}}(s), K^{\mathrm{fr}}(s)\right)$ composed of one controller for each axis (elevation, cross-elevation, field rotation)—the three controllers are decoupled because the action of the actuators on the line-of-sight angles are decoupled in Eq. (11); and the estimation parameters τ_1 and τ_2,
- The grey blocks are the weighting filters: $\mathbf{W}_d$ and $\mathbf{W}_n$ model the frequency content of the disturbances and of the noise respectively; $\mathbf{W}_u$, $\mathbf{W}_{e_d}$, $\mathbf{W}_{e_r}$ and $\mathbf{W}_{e_n}$ are the output weights used for the robust control synthesis,

Fig. 13 Closed-loop block diagram for the LOS pointing control

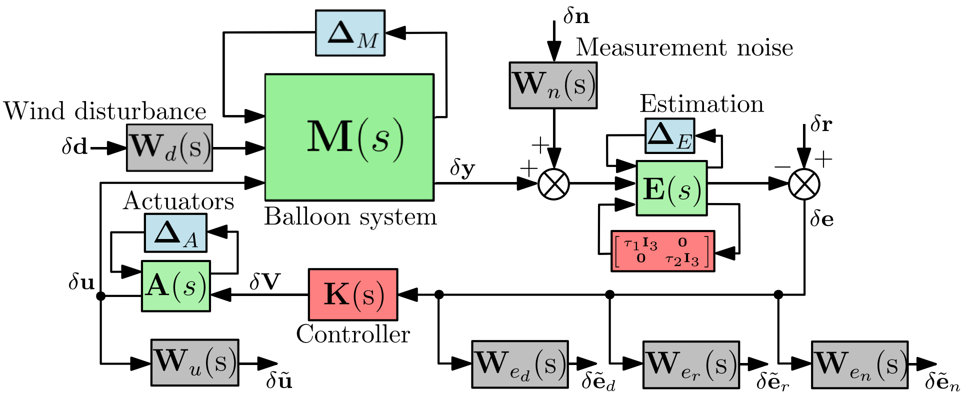

- The inputs are: the wind disturbances $\delta\mathbf{d} \in \mathbb{R}^2$ applied along $\mathbf{x}$ and $\mathbf{y}$ to the balloon; the sensors noises $\delta\mathbf{n} \in \mathbb{R}^6$; and the reference angles $\delta\mathbf{r} \in \mathbb{R}^3$,
- The internal signals are: the measured states $\delta\mathbf{y} \in \mathbb{R}^9$ regrouping the 3 gondola's rotation rates, the 3 actuators angles, and the 3 angles of the line-of-sight; the pointing error $\delta\mathbf{e} \in \mathbb{R}^3$; the actuators voltages $\delta\mathbf{V} \in \mathbb{R}^3$; and the commands $\delta\mathbf{u} = \delta\boldsymbol{\theta}^a \in \mathbb{R}^3$,
- The outputs are: the weighted errors $\delta\tilde{\mathbf{e}}_d \in \mathbb{R}^3$, $\delta\tilde{\mathbf{e}}_r \in \mathbb{R}^3$ and $\delta\tilde{\mathbf{e}}_n \in \mathbb{R}^3$, and the weighted command $\delta\tilde{\mathbf{u}} \in \mathbb{R}^3$.

The filter $D(s)$ obtained in Eq. (4) characterizes the wind disturbance:

$$\mathbf{W}_d(s) = D(s)\mathbf{I}_2 \tag{21}$$

and the measurement noise derives from Eq. (15):

$$\mathbf{W}_n(s) = \operatorname{diag}\left(\mathbf{W}_n^{\text{gyro}}, \mathbf{W}_n^{\text{optic}}\right). \tag{22}$$

4.3 Control requirements

One main objective of the pointing control is wind disturbance rejection. To improve the performance of the initial controller $\mathbf{K}_0(s)$, the filter $\mathbf{W}_{e_d}$ is defined to impose a maximum amplitude of $\epsilon_1 = 4 \times 10^{-5}$ rad in elevation/cross-elevation and $\epsilon_2 = 4 \times 10^{-3}$ rad in field rotation:

$$\mathbf{W}_{e_d} = \operatorname{diag}(1/\epsilon_1, 1/\epsilon_1, 1/\epsilon_2). \tag{23}$$

The reference tracking requirement—ensure a 30 rad/s (elevation and cross-elevation) or 5 rad/s (field rotation) bandwidth to follow a reference line-of-sight—yields the filter $\mathbf{W}_{e_r}$ which penalizes low-frequency error:

$$\mathbf{W}_{e_r} = \frac{1}{2}\operatorname{diag}\left(\frac{s+30}{s+0.03}, \frac{s+30}{s+0.03}, \frac{s+5}{s+0.005}\right) \tag{24}$$

and since $\mathbf{W}_{e_r}^{-1}$ imposes an upper bound on the closed-loop sensitivity function $\mathbf{S}$ (see Eq. (27)), and since the modulus margin r is such that $1/r = \|\mathbf{S}\|_\infty$, this requirement also ensures a modulus margin of at least 0.5. The limitation constraint of the actuators angles yields $\mathbf{W}_u$:

$$\mathbf{W}_u = 5 \times 10^5 \times \frac{s^2 + 0.56s + 0.16}{s^2 + 56s + 1600}\operatorname{diag}(1, 1, 1/20) \tag{25}$$

which penalizes high-frequency solicitation of the actuators and was computed to avoid degrading the performance of the initial controller with this regard. The pointing error caused by sensor noise is limited with the filter $\mathbf{W}_{e_n}$:

$$\mathbf{W}_{e_n} = 4 \times 10^5 \operatorname{diag}(1, 1, 1/40) \tag{26}$$

with a less stringent requirement on the field rotation due to the higher noise on this axis. This requirement also alleviates the fatigue of the actuators in response to the measurement noise. Finally, the controller is imposed to be stable. Let us note $\boldsymbol{\Delta} = \operatorname{diag}(\boldsymbol{\Delta}_M, \boldsymbol{\Delta}_A, \boldsymbol{\Delta}_E)$. The robust structured $\mathcal{H}_2/\mathcal{H}_\infty$ problem reads

$$\begin{array}{ll}\underset{\mathbf{K}(s),\tau_1,\tau_2}{\text{minimize}} & \gamma_1 = \max\limits_{\boldsymbol{\Delta}}\left\{\|\delta\mathbf{n} \to \delta\tilde{\mathbf{e}}_n\|_2\right\} < 1 \text{ (noise transmission)} \\ \text{subject to :} & \left\{\begin{array}{l}\gamma_2 = \max\limits_{\boldsymbol{\Delta}}\left\{\|\delta\mathbf{r} \to \delta\tilde{\mathbf{e}}_r\|_\infty\right\} < 1 \text{ (ref. tracking, stability margin)} \\ \gamma_3 = \max\limits_{\boldsymbol{\Delta}}\left\{\|\delta\mathbf{d} \to \delta\tilde{\mathbf{e}}_d\|_\infty\right\} < 1 \text{ (disturbance rejection)} \\ \gamma_4 = \max\limits_{\boldsymbol{\Delta}}\left\{\|\delta\mathbf{d} \to \delta\tilde{\mathbf{u}}\|_\infty\right\} < 1 \text{ (actuators solicitation)} \\ \text{s is a pole of } \mathbf{K} \implies \text{Re(s)} < 0 \text{ (stable controller).}\end{array}\right.\end{array} \tag{27}$$

Remark: The $\mathcal{H}_\infty$-norm is used in the performance indices γ_3 and γ_4, where the wind disturbance $\delta\mathbf{d}$ is the input, to minimize the resonances due to the flexible modes of the flight chain. The $\mathcal{H}_\infty$-norm is also used for the index γ_2 for the classical loop-shaping of the sensitivity function. On the other hand, since the $\mathcal{H}_2$-norm is convenient to quantify the standard deviation of the output signal when the input signal is random of unitary power spectral density (PSD), it is used for transfer between the sensors noise and the pointing error (the input has unitary PSD since the filter $\mathbf{W}_n$, integrated in the model, represents the frequency content).

4.4 Results

The problem (27) is solved with Matlab routine `systune` to ensure the robust stability and robust performance of the closed-loop system. The synthesis is initialized with the initial controller $\mathbf{K}_0(s)$ and the estimation parameters $\tau_1 = 0.1$ s and $\tau_2 = 0.5$ s. Each controller $K^{\mathrm{el}}(s), K^{\mathrm{ce}}(s), K^{\mathrm{fr}}(s)$ is a 3rd-order tunable controller, multiplied by the anti-aliasing filter defined in Eq. (17). Aside from the estimator, the only constraint regarding the structure of the controller was to have 3 decoupled controllers, as justified by Eq. (11); the order 3 was chosen as it was found to yield satisfying performance for a reasonable complexity.

Initial controller

The closed-loop transfers relative to the control requirements are presented in Fig. 14 with the initial controller $\mathbf{K}_0$ for 500 random samples, including the worst-case configurations identified by systune. The disturbance rejection objective (top left plot) is not met because of the natural resonances of the system (pendulum modes 1 and 2), and neither is the reference tracking/stability margin requirement with a critical frequency around 100 rad/s (bottom left plot). The two other control objectives are fulfilled: actuators solicitation (top right), transmission of sensor noise (bottom right—remark: the requirement is not represented since it is relative to the $\mathcal{H}_2$ norm).

Optimized controller and estimation parameters

The optimized controller is noted $\widehat{\mathbf{K}}(s)$ and the estimation parameters $\widehat{\tau}_1 = 0.17$ s and $\widehat{\tau}_2 = 8.0$ s are obtained. The closed-loop transfers are presented in Fig. 15 for 500

Fig. 14 Closed-loop transfers (500 samples) with $\mathbf{K}_0$

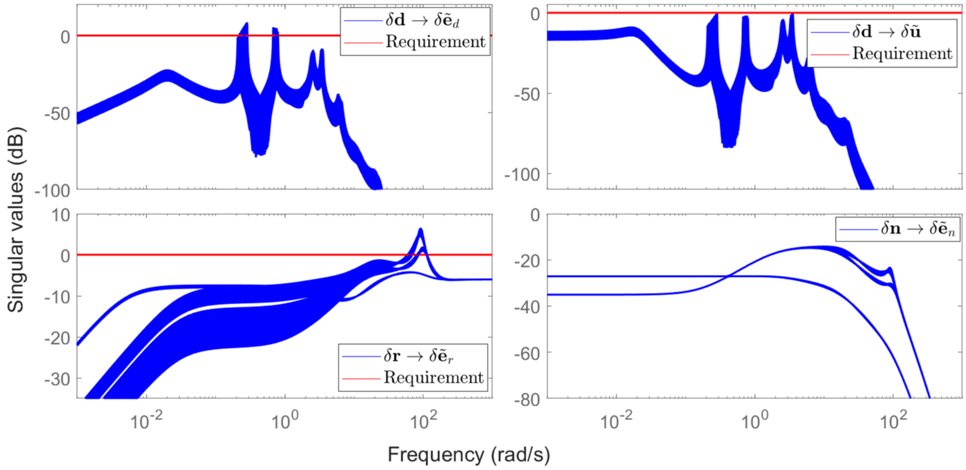

Fig. 15 Closed-loop transfers (500 samples) with $\widehat{\mathbf{K}}$

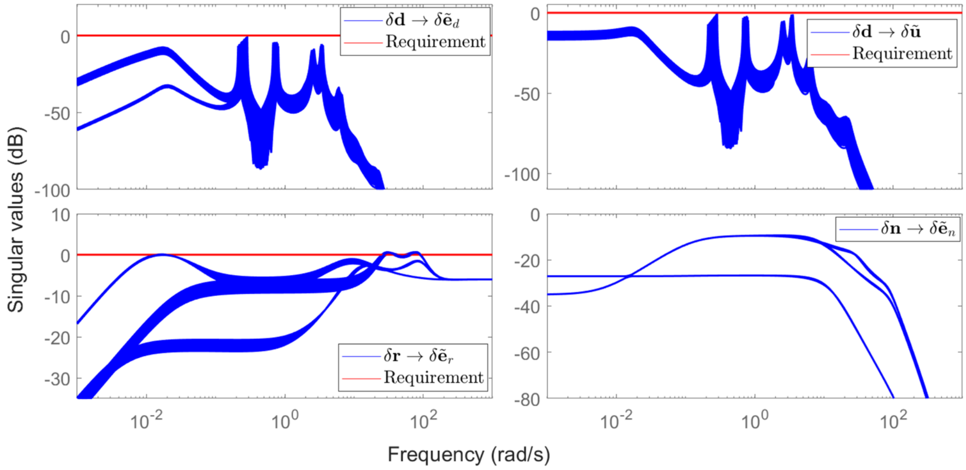

Table 2 Summary of the controllers performances

Type of variable	Variable name	Values		Comment
Decision variables	Controller	$\mathbf{K}_0$	$\widehat{\mathbf{K}}$	
	τ_1	0.1 s	0.17 s	
	τ_2	0.5 s	8.0 s	
Performance indices	γ_1	0.75	0.95	Noise transmission
	γ_2	2.13	1.09	Reference tracking
	γ_3	3.45	1.08	Disturbance rejection
	γ_4	1.08	1.08	Actuators solicitation
	r	0.25	0.49	Modulus margin

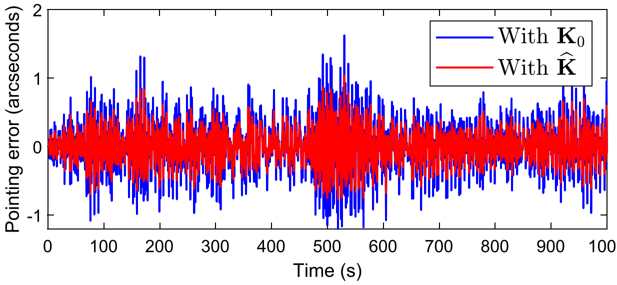

Fig. 16 Simulation: comparison of the controllers (elevation axis)

samples, including the worst-case configurations identified by systune. The control requirements are (almost) fulfilled.

Comparison of the controllers

The performance indices of the two controllers are summarized in Table 2. Essentially, the disturbance rejection γ_3 is improved, along with the reference tracking γ_2 (and consequently the modulus margin r), at the expense of the noise transmission γ_1. Some requirements are still slightly exceeded (value superior to 1), but this is deemed acceptable.

Remark: *The performance indices presented here are calculated after systune's heuristic evaluation of the worst-case configurations, which yields a lower bound of the actual worst-case performance. This point is addressed with μ-analysis in Sect. 5 for the disturbance rejection performance.*

The improvement on the disturbance rejection performance, represented by the index γ_3, is illustrated with a time-domain simulation. The response of the system to the wind disturbance, modeled as the colored noise presented in Sect. 2.3, is presented in Fig. 16 for the elevation axis.

The Bode plots, in magnitude and phase, of the two controllers $\mathbf{K}_0$ and $\widehat{\mathbf{K}}$ (tunable controller with anti-aliasing filter), are shown in Fig. 17.

5 Sensitivity analysis

This section focuses on the robust disturbance rejection performance, and its sensitivity to the uncertain parameters. Based on the LFT representation derived in this paper, the μ-analysis allows computing formal lower and upper bounds of the worst-case performance $\gamma_3 = \max_{\boldsymbol{\Delta}} \left\{ \|\delta\mathbf{d} \rightarrow \delta\tilde{\mathbf{e}}_d\|_\infty \right\}$:

$$\underline{\mu} < \gamma_3 < \overline{\mu}. \tag{28}$$

For this purpose, the SMAC/SMART toolbox [55, 56] is used throughout this section.

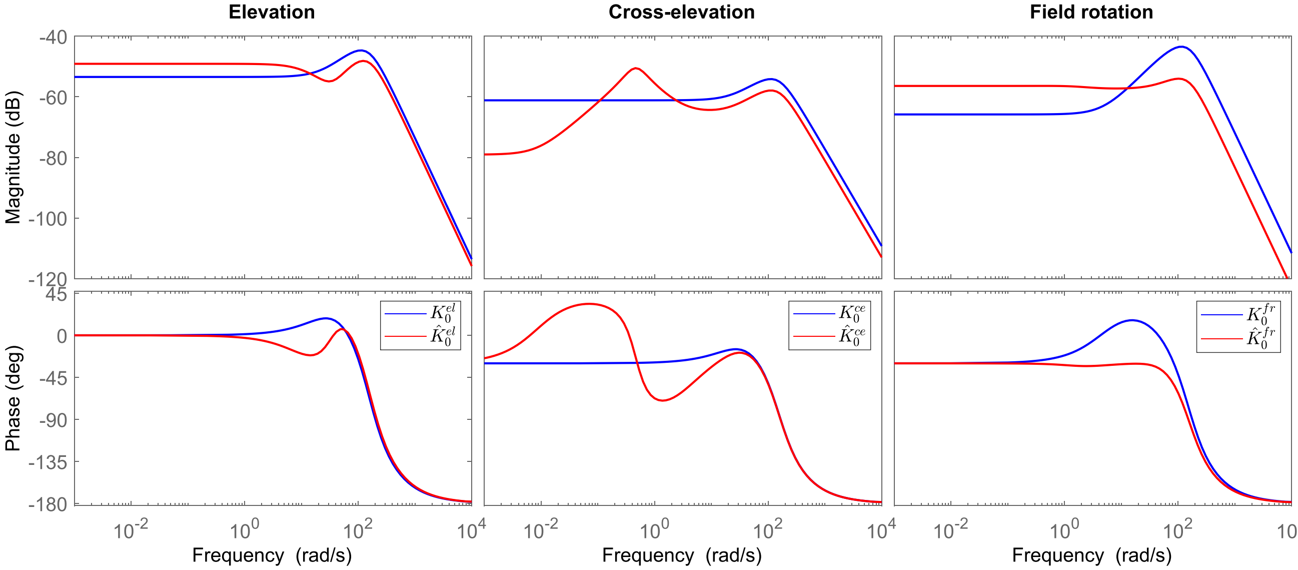

Fig. 17 Bode plots of the controllers $\mathbf{K}_0$ and $\widehat{\mathbf{K}}$

Table 3 Number of repetitions of the uncertain parameters

Element	Parameter	Number of repetitions
Balloon	Center of mass	4
	Center of buoyancy	2
	Center of pressure	2
	Mass	4
	Moment of inertia (x and y)	2
Gondola	Mass	32
	Center of mass	6
	Moment of inertia (x)	1
	Moment of inertia (y)	1
	Moment of inertia (z)	1
	Moment of inertia (xz)	2
	Ballast mass	32
Payload	Sensor delay t_o	15
	Actuator delay t_a	15
	Elevation angle t_{el}	16

However, μ-analysis methods are very sensitive to the size of the uncertain block $\mathbf{\Delta}$. Although a lower bound can be directly computed, at the critical frequency 0.30 rad/s (corresponding to the pendulum mode 1):

$$\underline{\mu} = 1.0843 \tag{29}$$

the computation of the upper bound did not converge. Indeed, the uncertain parameters exhibit a high number of repetitions, as shown in Table 3.

Therefore, a sensitivity analysis is proposed to reduce the model. The μ-sensitivity of a parameter measures the degradation of the worst-case performance when its uncertainty range varies. Let us define $\tilde{\mathbf{\Delta}}_i$ the parametric space such that the variation range of the i-th uncertain parameter around its nominal value is multiplied by $(1-\epsilon)$; the μ-sensitivity [57] is defined as

$$S_i = \left(\max_{\mathbf{\Delta}} \left\{ \|\delta \mathbf{d} \to \delta \tilde{\mathbf{e}}_d\|_\infty \right\} - \max_{\tilde{\mathbf{\Delta}}_i} \left\{ \|\delta \mathbf{d} \to \delta \tilde{\mathbf{e}}_d\|_\infty \right\} \right) / \epsilon. \tag{30}$$

Lower bounds are used to compute the μ-sensitivity, since the actual worst-case performance or an upper bound cannot be computed. The value $\epsilon = 0.1$ is used. The results are presented in Fig. 18.

Then, a reduced system is defined by only keeping the seven most impacting uncertain parameters to enable the computation of an upper bound. The other eight parameters are set to their worst-case value identified in the computation of the lower bound in Eq. (29).

The worst-case performance of the reduced system is noted $\tilde{\gamma}_3$. It verifies $\tilde{\gamma}_3 \leq \gamma_3$, but since the most sensitive parameters were retained, it can be expected that $\tilde{\gamma}_3 \approx \gamma_3$. We now search to compute bounds for the reduced system:

$$\underline{\tilde{\mu}} < \tilde{\gamma}_3 < \tilde{\tilde{\mu}} \tag{31}$$

and, accordingly to the critical frequencies identified in the sensitivity analysis, the frequency range is limited to [0.25–0.4] rad/s to ease the following computations. As for the full system, a lower bound can be directly computed:

$$\underline{\tilde{\mu}} = 1.0843. \tag{32}$$

However, since the gondola mass and the ballast mass are still repeated 32 times each:

- the gondola mass is set to the worst-case value identified in the computation of the lower bound;
- the ballast mass is discretized across its variation range, to assess the impact of the release of ballast during the flight.

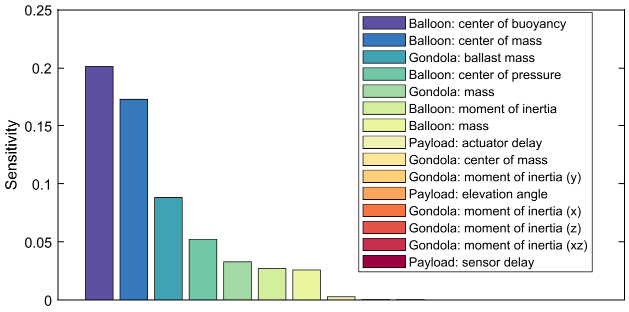

Fig. 18 Sensitivity to the uncertain parameters

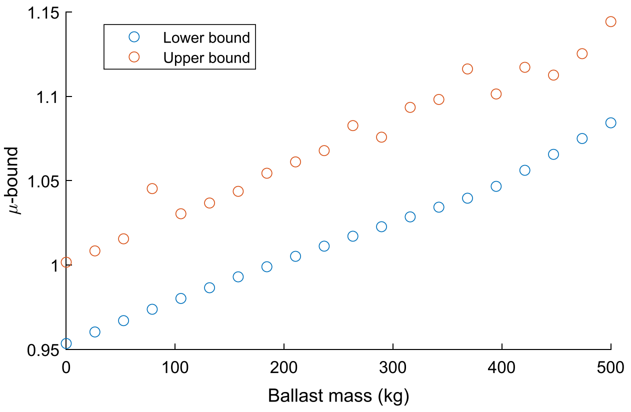

Fig. 19 Lower and upper bounds of the reduced model

The resulting lower and upper bounds, as a function of the ballast mass, are presented in Fig. 19. The lower and upper bounds are close to each other, so they provide a good evaluation of the performance. Overall, the performance is improved when the ballast mass decreases. The objective (value 1) is guaranteed for a ballast mass of zero (upper bound equal to 1), and it is necessarily exceeded for a ballast mass superior to 200 kg (lower bound superior to 1).

6 Conclusion

A first dynamical model was proposed based on Lagrangian mechanics. This method is easy to apply for any flight chain, yet was shown to provide a good prediction of the frequency content of the platform's motion when applied to the Faint Intergalactic-medium Redshifted Emission Balloon (FIREBall) experiment and validated with flight data, in particular regarding the flexible pendulum-like modes. Then, an LFT model was derived based on a general multibody approach to take into account parametric uncertainties such as the ballast mass or the balloon's mechanical parameters.

Based on the model of the system, the structured $\mathcal{H}_2/\mathcal{H}_\infty$ control framework was chosen to address the line-of-sight pointing control. Indeed, it allows reducing the amplification of the flexible modes, which are the main source of pointing error according to the model and to the flight experience, while ensuring other constraints in the frequency domain such as the control bandwidth, the modulus margin, or actuators limitation. Moreover, this method takes into account parametric uncertainties since the performance is optimized with regard to the worst-case parametric configurations. It was shown that this approach improved the performance with regard to an initial controller that was tuned with a traditional PID approach which did not fully take advantage of the knowledge of the system (sensors noise and delays, actuators dynamics, natural frequencies, etc.).

Declarations

Conflict of interest The authors declare that they have no conflict of interest.

References

1. Yajima, N., Imamura, T., Izutsu, N., Abe, T.: Scientific Ballooning: Technology and Applications of Exploration Balloons Floating in the Stratosphere and the Atmospheres of Other Planets, pp. 12–14. Springer, New York (2009). https://doi.org/10.1007/978-0-387-09727-5
2. Montel, J., Pérot, E., Mirc, F., Evrard, J., Melso, N., Schiminovich, D.: FIREBALL-2 (2018) in-flight pointing performance. In: 24th ESA Symposium on European Rocket and Balloon Programmes and Related Research, pp. 51–57. ESA publications, Essen (2019)
3. Rhodes, J., Dobke, B., Booth, J., Massey, R., Liewer, K., Smith, R., Amara, A., Aldrich, J., Berge, J., Bezawada, N., Brugarolas, P., Clark, P., Dubbeldam, C.M., Ellis, R., Frenk, C., Gallie, A., Heavens, A., Henry, D., Jullo, E., Kitching, T., Lanzi, J., Lilly, S., Lunney, D., Miyazaki, S., Morris, D., Paine, C., Peacock, J., Pellegrino, S., Pittock, R., Pool, P., Refregier, A., Seiffert, M., Sharples, R., Smith, A., Stuchlik, D., Taylor, A., Teplitz, H., Ali Vanderveld, R., Wu, J.: Space-quality data from balloon-borne telescopes: the High Altitude Lensing Observatory (HALO). Astropart. Phys. (1), 31–40 (2012). https://doi.org/10.1016/j.astropartphys.2012.05.015. arXiv:1205.2957
4. Young, E.F., Mellon, R., Percival, J.W., Jaehnig, K.P., Fox, J., Lachenmeier, T., Oglevie, B., Bingenheimer, M.: Sub-arcsecond performance of the ST5000 star tracker on a balloon-borne platform. In: IEEE Aerospace Conference Proceedings, pp. 1–7 (2012). https://doi.org/10.1109/AERO.2012.6187179
5. Diller, J., Dinkel, K., Dischner, Z., Young, E.: Design and performance of the BOPPS UVVis fine pointing system. In: IEEE Aerospace Conference Proceedings, pp. 1–12 (2015). https://doi.org/10.1109/AERO.2015.7119125
6. Mendillo, C.B., Hewawasam, K., Howe, G.A., Martel, J., Cook, T.A., Chakrabarti, S.: The PICTURE-C exoplanetary direct imaging balloon mission: first flight preparation. In: Proceedings of SPIE (2019). https://doi.org/10.1117/12.2529710
7. Hamden, E., Martin, D.C., Milliard, B., Schiminovich, D., Nikzad, S., Evrard, J., Kyne, G., Grange, R., Montel, J., Pirot, E., Hoadley, K., O'sullivan, D., Melso, N., Picouet, V., Vibert, D., Balard, P., Blanchard, P., Crabill, M., Pascal, S., Mirc, F., Bray, N., Jewell, A., Blue Bird, J., Zorilla, J., Ong, H.R., Matuszewski, M., Lingner, N., Augustin, R., Limon, M., Gomes, A., Tapie, P., Soors, X., Zenone, I., Saccoccio, M.: FIREBall-2: the faint intergalactic medium redshifted emission balloon telescope. Astrophys. J. (2) (2020). https://doi.org/10.3847/1538-4357/aba1e0. arXiv:2007.08528v1
8. Howe, G.A., Mendillo, C.B., Hewawasam, K., Chakrabarti, S., Cook, T.A., Martel, J., Finn, S.C.: The low-order wavefront control system for the PICTURE-C mission: preliminary testbed results from the Shack–Hartmann sensor. In: Proceedings of SPIE—The International Society for Optical Engineering (2017). https://doi.org/10.1117/12.2274122
9. Romualdez, L.J., Benton, S.J., Brown, A.M., Clark, P., Damaren, C.J., Eifler, T., Fraisse, A.A., Galloway, M.N., Gill, A., Hartley, J.W., Holder, B., Huff, E.M., Jauzac, M., Jones, W.C., Lagattuta, D., Leung, J.S.Y., Li, L., Luu, T.V.T., Massey, R.J., McCleary, J., Mullaney, J., Nagy, J.M., Netterfield, C.B., Redmond, S., Rhodes, J.D., Schmoll, J., Shaaban, M.M., Sirks, E., Tam, S.I.: Robust diffraction-limited near-infrared-to-near-ultraviolet wide-field imaging from stratospheric balloon-borne platforms—super-pressure Balloon-borne Imaging Telescope performance. Rev. Sci. Instrum. (3) (2020). https://doi.org/10.1063/1.5139711
10. Nigro, N.J.: Attitude determination of a high altitude balloon system. Part 1: Development of the mathematical model. Technical report, NASA-CR-142193 (1975)
11. Nigro, N.J., Nimityongskul, P., Hintor, D.E.: Improved method for predicting attitude of balloon gondolas. Technical report (1978)
12. Nigro, N.J.: Feasibility of observer system for determining orientation of balloon borne observational platform. Technical report, NASA-CR-168945 (1982)
13. Nigro, N.J., Yang, J.K., Elkouh, A.F., Nigro, N.J.: Generalized math model for simulation of high-altitude balloon systems. J. Aircr. **22**(8), 697–704 (1985). https://doi.org/10.2514/3.45189
14. White, J.E., Etter, J.R.: Linear-quadratic-regulator pointing control system for a high-altitude balloon payload. J. Guid. Control Dyn. **13**(4), 615–623 (1990). https://doi.org/10.2514/3.25378

15. Chingcuanco, A.O., Lubin, P.M., Meinhold, P.R., Tomizuka, M.: Modeling and control of a balloon borne stabilized platform. J. Dyn. Syst. Meas. Control **4**, 703–710 (1990). https://doi.org/10.1115/1.2896198
16. Chingcuanco, A.O., Lubin, P.M., Meinhold, P.R., Tomizuka, M.: Model reference adaptive control for the azimuth-pointing system of a balloon-borne stabilized platform. Int. J. Adapt. Control Signal Process. **2**, 107–120 (1991). https://doi.org/10.1002/acs.4480050204
17. Matko, D., Yajima, N., Hinada, M.: Adaptive stabilisation of lateral motion of a balloon gondola. Control Eng. Pract. **5**(6), 763–769 (1997). https://doi.org/10.1016/S0967-0661(97)00060-9
18. Ward, P.R., DeWeese, K.D.: Balloon borne arcsecond pointer feasibility study. In: 16th ESA Symposium on European Rocket and Balloon Programmes and Related Research, pp. 197–205. ESA Publications, St. Gallen (2003)
19. Sakamoto, Y., Kanazawa, T., Shouji, Y., Takahashi, Y., Yoshida, K., Taguchi, M.: Dynamic modeling and experimental verification of the pointing technology in balloon-borne telescope system for optical remote sensing of planets. Trans. Jpn. Soc. Aeronaut. Space Sci. Space Technol. Jpn. **7**(26), 23–28 (2009). https://doi.org/10.2322/tstj.7.pd_23
20. Nakano, T., Shoji, Y., Yamamoto, M., Hamamoto, K., Nakamoto, J., Imai, M., Sakamoto, Y., Kuwahara, T., Watanabe, M., Takahashi, Y., Yoshida, K., Taguchi, M.: The pointing control method of balloon-borne telescope compensating the motion of flexible base. In: IEEE/SICE International Symposium on System Integration, pp. 313–318. IEEE, Fukuoka (2012). https://doi.org/10.1109/SII.2012.6427318
21. Nakano, T.: Design of attitude control system for stratospheric balloon gondolas by sliding mode control. In: Conference on Mechanical Engineering, vol. 501. IOP Conference Series: Materials Science and Engineering, Phuket, Thailand (2019). https://doi.org/10.1088/1757-899X/501/1/012010
22. Zhang, D., Zhou, J., Huang, W.: Design of decoupling control system for the azimuth control of balloon-borne mission. In: 35th Chinese Control Conference. IEEE, Chengdu (2016). https://doi.org/10.1109/ChiCC.2016.7555071
23. Fissel, L.M.: PHD thesis—probing the role played by magnetic fields in star formation with BLASTPol. PhD thesis (2013)
24. Aubin, F., Bayman, B., Hanany, S., Franco, H., Marsh, J., Didier, J., Miller, A.D.: Torsional balloon flight line oscillations: comparison of modelling to flight data. Adv. Space Res. **60**(3), 702–708 (2017). https://doi.org/10.1016/j.asr.2017.05.003
25. Quadrelli, M.B., Cameron, J.M., Kerzhanovich, V.: Multibody dynamics of parachute and balloon flight systems for planetary exploration. J. Guid. Control Dyn. **4**, 564–571 (2004). https://doi.org/10.2514/1.11374
26. Romualdez, L.J.: Design, implementation, and operational methodologies for sub-arcsecond attitude determination, control, and stabilization of the super-pressure balloon-borne imaging telescope (SuperBIT). PhD thesis (2018)
27. Smith, I.S., Chaffee, E.A., Noll, J.R., Martin, B.A.: The investigation and measurement of balloon dynamics at the apex and base of a scientific balloon. In: AIAA Balloon Systems Conference, p. 3286. AIAA, Denver (2017). https://doi.org/10.2514/6.2017-3286
28. Kassarian, E., Sanfedino, F., Alazard, D., Evain, H., Montel, J.: Modeling and stability of balloon-borne gondolas with coupled pendulum-torsion dynamics. Aerosp. Sci. Technol. (2021). https://doi.org/10.1016/j.ast.2021.106607
29. Kassarian, E., Sanfedino, F., Alazard, D., Chevrier, C.-A., Montel, J.: Linear Fractional Transformation modeling of multibody dynamics around parameter-dependent equilibrium. IEEE Trans. Control Syst. Technol. (2022). https://doi.org/10.1109/TCST.2022.3167610
30. DeWeese, K.D., Ward, P.R.: Demonstration of a balloon borne arc-second pointer design. In: 36th COSPAR Scientific Assembly, Beijing (2006)
31. Varga, D.M., Dischner, Z.: Current status of a NASA high-altitude balloon-based observatory for planetary science. In: AIAA Balloon Systems Conference 2015, MBAL 2015—Held at the AIAA Aviation Forum 2015, pp. 1–9 (2015). https://doi.org/10.2514/6.2015-3040
32. Stuchlik, D.W.: The wallops arc second pointer—a balloon borne fine pointing system. In: AIAA Balloon Systems Conference 2015, MBAL 2015—Held at the AIAA Aviation Forum 2015 (June), pp. 1–15 (2015). https://doi.org/10.2514/6.2015-3039
33. Benford, D.J., Fixsen, D.J., Rinehart, S.A., Rizzo, M., Maher, S.F., Barry, R.K.: Precision attitude control for the BETTII balloon-borne interferometer. In: Ground-Based and Airborne Telescopes IV (October 2012), p. 84442 (2012). https://doi.org/10.1117/12.927224
34. Hawat, T.M., Torguet, R.J., Camy-Peyret, C., Jeseck, P., Payan, S.: Pointing and sun-tracker system for the LPMA gondola. In: Proceedings of SPIE—The International Society for Optical Engineering (June 1996), pp. 112–119 (1996). https://doi.org/10.1117/12.241908
35. Nakano, T., Sakamoto, Y., Yoshida, K., Kuwahara, T., Shoji, Y., Taguchi, M., Yamamoto, M., Takahashi, Y.: The balloon-borne telescope system for optical observation of planets. In: 2010 IEEE/SICE International Symposium on System Integration: SI International 2010—The 3rd Symposium on System Integration, SII 2010, Proceedings, pp. 236–241 (2010). https://doi.org/10.1109/SII.2010.5708331
36. Shariff, J.A., Ade, P.A.R., Amiri, M., Benton, S.J., Bock, J.J., Bond, J.R., Bryan, S.A., Chiang, H.C., Contaldi, C.R., Crill, B.P., Doré, O.P., Farhang, M., Filippini, J.P., Fissel, L.M., Fraisse, A.A., Gambrel, A.E., Gandilo, N.N., Golwala, S.R., Gudmundsson, J.E., Halpern, M., Hasselfield, M., Hilton, G.C., Holmes, W.A., Hristov, V.V., Irwin, K.D., Jones, W.C., Kermish, Z.D., Kuo, C.L., MacTavish, C.J., Mason, P.V., Megerian, K.G., Moncelsi, L., Morford, T.A., Nagy, J.M., Netterfield, C.B., O'Brient, R., Rahlin, A.S., Reintsema, C.D., Ruhl, J.E., Runyan, M.C., Soler, J.D., Trangsrud, A., Tucker, C.E., Tucker, R.S., Turner, A.D., Weber, A.C., Wiebe, D.V., Young, E.Y.: Pointing control for the SPIDER balloon-borne telescope. SPIE **9145**(July 2014), 91450 (2014). https://doi.org/10.1117/12.2055166. arXiv:1407.1880
37. Diller, J., Dinkel, K., Dischner, Z., Truesdale, N., Young, E.: Design and performance of the BBRISON UV–VIS fine pointing system. In: IEEE Aerospace Conference Proceedings, pp. 1–11 (2014). https://doi.org/10.1109/AERO.2014.6836329
38. Shoji, Y., Taguchi, M., Nakano, T., Maeda, A., Imai, M., Gouda, Y., Watanabe, M., Takahashi, Y., Sakamoto, Y., Yoshida, K.: FUJIN-2: balloon borne telescope for optical observation of planets. Transactions of the Japan Society for Aeronautical and Space Sciences, Aerospace Technology Japan (2016)
39. Jones-Wilson, L., Susca, S., Diaz, C., Chang, H., Duffy, E., Effinger, R., Lewis, D., Liewer, K., Lo, K., Ochoa, H., Perez, J., Rizvi, A., Seubert, C., Umsted, C., Borden, M., Clark, P., Massey, R., Porter, M.: A sub-arcsecond pointing stability fine stage for a high altitude balloon platform. In: IEEE Aerospace Conference Proceedings (2017). https://doi.org/10.1109/AERO.2017.7943590
40. Quine, B.M., Strong, K., Wiacek, A., Wunch, D., Anstey, J.A., Drummond, J.R.: Scanning the earth's limb from a high-altitude balloon: the development and flight of a new balloon-based pointing system. J. Atmos. Ocean. Technol. **5**, 618–632 (2002). https://doi.org/10.1175/1520-0426(2002)019<0618:STESLF>2.0.CO;2
41. Romualdez, L.J., Damaren, C.J., Li, L. et al.: Precise pointing and stabilization performance for the balloon-borne imaging testbed:

2015 test flight. Proceedings of the Institution of Mechanical Engineers, Part G: J. Aerosp. Eng. **231**, 713–727 (2017) https://doi.org/10.1177/0954410016641451

42. Aboobaker, A., Ade, P., Araujo, D., Aubin, F., Baccigalupi, C., Bao, C., Chapman, D., Didier, J., Dobbs, M., Grainger, W., Hanany, S., Helson, K., Hillbrand, S., Hubmayr, J., Jaffe, A., Johnson, B., Jones, T., Klein, J., Korotkov, A., Lee, A., Levinson, L., Limon, M., MacDermid, K., Miller, A.D., Milligan, M., Moncelsi, L., Pascale, E., Raach, K., Reichborn-Kjennerud, B., Sagiv, I., Tucker, C., Tucker, G.S., Westbrook, B., Young, K., Zilic, K.: The EBEX balloon-borne experiment-gondola, attitude control, and control software. Astrophys. J. Suppl. Ser. (1), 9 (2018). https://doi.org/10.3847/1538-4365/aae435. arXiv:1702.07020
43. Montel, J., Mirc, F., Pérot, E., Zenone, I., Nicot, J.-M., Bray, N., Gomes, A., Evrard, J., Tapie, P., Vola, P., Milliard, B., Grange, R., Schiminovich, D.: Design and improvements of the Attitude Control System of the FIREBall balloon experiment. SPIE (July 2016), 99053 (2016). https://doi.org/10.1117/12.2236224
44. Makto, D., Yajima, N., Hinada, M.: Adaptive balloon azimuth control using a simple DC motor actuator. Technical report (1996)
45. Honghui, W., Zhaohui, Y., Juan, W.: Research on a new azimuth control method for stratospheric balloon-borne gondola system. In: Applied Mechanics and Materials, vol. 190–191, pp. 1033–1039 (2012). https://doi.org/10.4028/www.scientific.net/AMM.190-191.1033
46. Apkarian, P., Noll, D.: Nonsmooth H infinity synthesis. IEEE Trans. Autom. Control **1**, 71–86 (2006)
47. Apkarian, P., Dao, M.N., Noll, D.: Parametric robust structured control design. IEEE Trans. Autom. Control (7), 1857–1869 (2015). https://doi.org/10.1109/TAC.2015.2396644. arXiv:1405.4202
48. Apkarian, P., Noll, D.: The H infinity control problem is solved. Aerosp. Lab (13), 1–27 (2006). https://doi.org/10.12762/2017.AL13-01
49. Apkarian, P., Noll, D.: Nonsmooth optimization for multidisk H infinity synthesis. Eur. J. Control **3**, 229–244 (2006). https://doi.org/10.3166/ejc.12.229-244
50. Hoblit, F.M.: Gust Loads on Aircraft: Concepts and Applications. AIAA Education Series, Washington (1988). https://doi.org/10.2514/4.861888
51. Flying qualities of piloted aircraft. Technical report. US Department of Defense, Washington (1990)
52. Treilhou, J.P., Coutelier, J., Thocaven, J.J., Jacquey, C.: Payload motions detected by balloon-borne fluxgate-type magnetometers. Adv. Space Res. **9**, 1423–1426 (2000)
53. Alexander, P., De La Torre, A.: Uncertainties in the measurement of the atmospheric velocity due to balloon-gondola pendulum-like motions. Adv. Space Res. **4**, 736–739 (2011). https://doi.org/10.1016/j.asr.2010.09.020
54. Dubanchet, V.: Modeling and control of a flexible space robot to capture a tumbling debris. PhD thesis, Ecole Polytechnique de Montréal (2016)
55. J-M. Biannic, L. Burlion, F. Demourant, G. Ferreres, G. Hardier, T. Loquen and C. Roos, "The SMAC Toolbox: a collection of libraries for Systems Modeling, Analysis and Control", June 2016, online available at http://w3.onera.fr/smac/
56. C. Roos, "Systems Modeling, Analysis and Control (SMAC) toolbox: an insight into the robustness analysis library", in Proceedings of the IEEE Multiconference on Systems and Control, Hyderabad, India, August 2013, pp. 176–181, available with the SMAC toolbox at http://w3.onera.fr/smac/smart
57. Braatz, R.D., Morari, M.: mu-sensitivities as an aid for robust identification. In: 1991 American Control Conference, pp. 231–236 (1991). https://doi.org/10.23919/ACC.1991.4791363